CrossMark

electronic reprint

FOUNDATIONS
ADVANCES

ISSN: 2053-2733
journals.iucr.org/a

Bragg–von Laue diffraction generalized to twisted X-rays

Dominik Jüstel, Gero Friesecke and Richard D. James

Acta Cryst. (2016). A**72**, 190–196

IUCr Journals
CRYSTALLOGRAPHY JOURNALS ONLINE

Copyright © International Union of Crystallography

Author(s) of this paper may load this reprint on their own web site or institutional repository provided that this cover page is retained. Republication of this article or its storage in electronic databases other than as specified above is not permitted without prior permission in writing from the IUCr.

For further information see http://journals.iucr.org/services/authorrights.html

FOUNDATIONS ADVANCES

ISSN 2053-2733

Bragg–von Laue diffraction generalized to twisted X-rays

Dominik Jüstel,[a] Gero Friesecke[a]* and Richard D. James[b]*

[a]Department of Mathematics, TU Munich, Germany, and [b]Department of Aerospace Engineering and Mechanics, University of Minnesota, USA. *Correspondence e-mail: gf@ma.tum.de, james@umn.edu

Received 22 October 2015
Accepted 18 December 2015

Edited by D. A. Keen, STFC Rutherford Appleton Laboratory, UK

Keywords: X-ray diffraction; structure determination; noncrystalline structures; twisted X-rays.

A pervasive limitation of nearly all practical X-ray methods for the determination of the atomic scale structure of matter is the need to crystallize the molecule, compound or alloy in a sufficiently large ($\sim 10 \times 10 \times 10\,\mu m$) periodic array. In this paper an X-ray method applicable to structure determination of some important noncrystalline structures is proposed. It is designed according to a strict mathematical analog of von Laue's method, but replacing the translation group by another symmetry group, and simultaneously replacing plane waves by different exact closed-form solutions of Maxwell's equations. Details are presented for helical structures like carbon nanotubes or filamentous viruses. In computer simulations the accuracy of the determination of structure is shown to be comparable to the periodic case.

1. Introduction

Since its discovery by von Laue (Friedrich *et al.*, 1912) and its early exploitation as a method for the determination of the structures of simple crystals by the Braggs (Bragg, 1913), X-ray diffraction as a method of structure determination has dominated structural research in materials science and biology. However, many of the most important materials whose structure is unknown do not readily crystallize as three-dimensional periodic structures and, furthermore, a crystallized protein or nanostructure may lose critical function due to confinement or processing conditions for crystallization. Even well known simple nanostructures, such as carbon nanotubes, do not have accurately characterized lattice parameters due to the combined effects of mixed chiralities and long period cells.

The more recent method of coherent diffractive imaging (CDI) (Miao *et al.*, 1999) is applicable to general structures, but the absence of constructive/destructive interference gives lower resolution than classical X-ray methods. This shortcoming is shared by fiber diffraction methods (Cochran *et al.*, 1952; Stubbs, 2001) for helical structures, which lead to sharp signals only in an axial but not angular direction. Structure reconstruction from non-sharp signals was recently reviewed by Keen & Goodwin (2015).

The fundamental reason periodic X-ray diffraction is so remarkably effective, and conventionally gives diffraction patterns with peaks that differ from the background by two to four orders of magnitude, arises from the conspiring effects of constructive and destructive interference. Constructive interference arises because a large fraction of atoms in the sample are positioned to resonate with the incoming wave. Destructive interference, which results in unexpectedly dramatic cancellation of the outgoing field of even slightly off-resonance incoming waves, is more subtle, and is explained

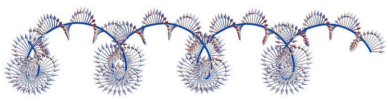

© 2016 International Union of Crystallography

electronic reprint

mathematically by a fundamental theorem in Fourier analysis, the Poisson summation formula (Strichartz, 2003).

For noncrystalline but symmetric structures suitable radiation can be designed by exploiting a powerful mathematical analogy that has not been previously noticed. To explain this analogy, we first focus on the periodic case. Based on the Bragg picture, constructive/destructive interference occurs because the incoming wave is periodic, and also the structure is periodic. A closer examination reveals that, in fact, the hypothesis of periodicity is not fundamentally what is being used, but rather a group structure. The key point is that the structure being interrogated is the orbit of a discrete symmetry group, and the incoming radiation has a matching symmetry. Here 'matching symmetry' of the radiation means not just the same discrete symmetry as the structure, but a symmetry related to a larger, *continuous*, symmetry group, so as to give destructive interference when the radiation parameters or structure constants are tuned such that the outgoing waves are off-resonance. This leads to 'design equations' for the incoming radiation [equations (4), (6) in Appendix *A*].

Our method of radiation design works in principle for any structure that is the orbit of one to thousands of atom positions under a discrete subgroup of the Euclidean group of rotations (proper or improper) and translations. Remarkably, some of the most important structures in biology, and a strikingly disproportionate number of structures emerging in nanoscience, are of this type. Examples include buckyballs and many fullerenes, the parts of many viruses, actin, carbon nanotubes (all chiralities), graphene and a large collection of other two-dimensional structures, such as the currently important structures black phosphorus and the dichalcogenides. It is not understood from a fundamental viewpoint why such structures (the orbits of a few atoms under a discrete Euclidean group) occur so frequently, but it is likely to be related to the invariance exploited here. The associated mathematical problem is the celebrated, and far from solved, 'crystallization problem'.

In this paper we do not report the design and construction of an X-ray machine suitable for the production of the relevant incoming radiation and the sensing of the peaks. However, our theoretical results are completely explicit, without undetermined parameters, and could be used as a basis for contemplating an actual design. Our goal is to explain the basic theory in a form intended to motivate the search for possible designs among groups with expertise in experimental design.

2. Twisted X-rays

We now present the details for the important special case of helical structures, choosing suitable radiation according to our design. The general solution of our design equations [equation (7)] for these helical structures is

$$\mathbf{E}(r,\varphi,z,t) = \exp[i(\alpha\varphi+\beta z-\omega t)] \times \begin{pmatrix} \cos\varphi & -\sin\varphi & 0 \\ \sin\varphi & \cos\varphi & 0 \\ 0 & 0 & 1 \end{pmatrix} \begin{pmatrix} \frac{n_1+in_2}{2} & \frac{n_1-in_2}{2} & 0 \\ \frac{n_2-in_1}{2} & \frac{n_2+in_1}{2} & 0 \\ 0 & 0 & n_3 \end{pmatrix} \begin{pmatrix} J_{\alpha+1}(\gamma r) \\ J_{\alpha-1}(\gamma r) \\ J_\alpha(\gamma r) \end{pmatrix}, \tag{1}$$

where $\mathbf{E}(r,\varphi,z,t)$ is the electric field at the point defined by cylindrical coordinates r,φ,z at time t, $\mathbf{n}=(n_1,n_2,n_3)$ is a (generally complex) vector satisfying $\mathbf{n}\cdot(0,\gamma,\beta)=0$, J_σ is a Bessel function of order σ, ω is the frequency, and the integer α and real numbers $\beta,\gamma>0$ are parameters closely analogous to the wavevector $\mathbf{k}$ of plane waves. These parameters are related to the frequency by $(\gamma^2+\beta^2)^{1/2}=\omega/c$, where c is the speed of light. We call waves given by equation (1) *twisted waves*. Fig. 1 shows a picture of a generic twisted wave with the electric field vectors plotted along the direction of energy flux. Together with the associated magnetic field, which is also of the form of equation (1) but with $\mathbf{n}$ replaced by $(1/\omega)(0,\gamma,\beta)\times\mathbf{n}$, twisted waves are exact solutions of time-harmonic Maxwell's equations in free space.

These twisted-wave solutions have the fascinating property of exhibiting orbital angular momentum (OAM). This, together with the fact that we need a large set of twisted waves to obtain a sufficient number of peaks in the scattered radiation to fully recover any helical structure, provides additional motivation for ongoing research on OAM beams and photons (Allen *et al.*, 1992; Arlt & Dholakia, 2000; Molina-Terriza *et al.*, 2007). Related research is underway in electron microscopy following the recent creation of electron vortex beams

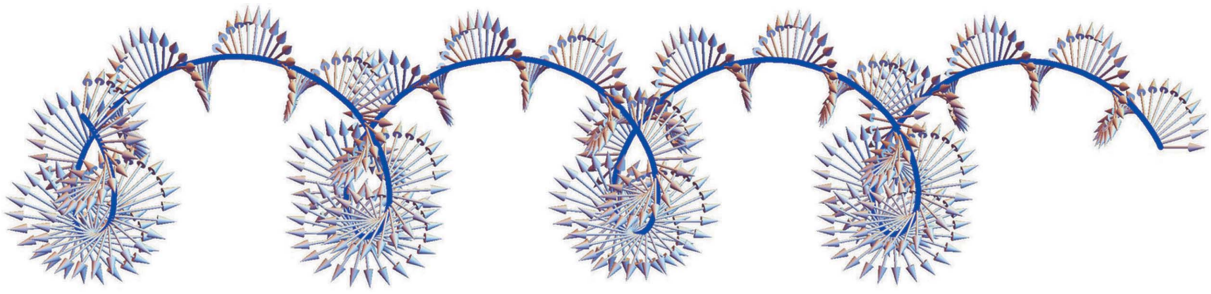

Figure 1
A twisted wave with angular, axial and radial wavenumbers $(\alpha,\beta,\gamma)=(2,1.63,1)$. The electric field vectors are plotted along a helix whose tangent is the Poynting vector, *i.e.* the direction of energy flux. Twisted waves are general solutions of our design equations and therefore are suitable for structure determination of helical structures.

electronic reprint

(Uchida & Tonomura, 2010; Verbeeck *et al.*, 2010; Juchtmans *et al.*, 2015; Juchtmans & Verbeeck, 2015; van Veenendaal & McNulty, 2007). The waveform (1) differs somewhat from previously reported OAM waveforms. Scalar high-order Bessel beams as reported in Arlt & Dholakia (2000) describe the individual twisted-wave components but not their interplay. The Laguerre–Gauss vector beam reported in Allen *et al.* (1992) exhibits a different variation of the polarization direction with cylindrical angle. If one neglects localization effects (as justified in our context of atomic scale X-ray imaging) the latter beam reduces to a Hansen harmonic (Hansen, 1937) curl $\mathbf{a}\exp[i(\alpha\varphi+\beta z-\omega t)J_\alpha(\gamma r)$. Interestingly, if in addition one replaces the transversal (Allen *et al.*, 1992) choice of $\mathbf{a}$ by an axial one, the resulting Hansen harmonic can be written in the form of equation (1); but any other choice of $\mathbf{a}$ does not yield a twisted wave, and conversely any other twisted wave is not of this Hansen form. Such differences will influence some details of the diffraction signals, but our analysis shows that they will not undermine the basic phenomenon of discrete diffraction peaks.

There remain two key tasks. First, we have to demonstrate that the scattered radiation exhibits constructive/destructive interference by precisely the same mechanism as plane waves do for crystals, as claimed above. Second, we have to give an explicit procedure for recovery of the structure by measurement of the peaks in the scattered radiation.

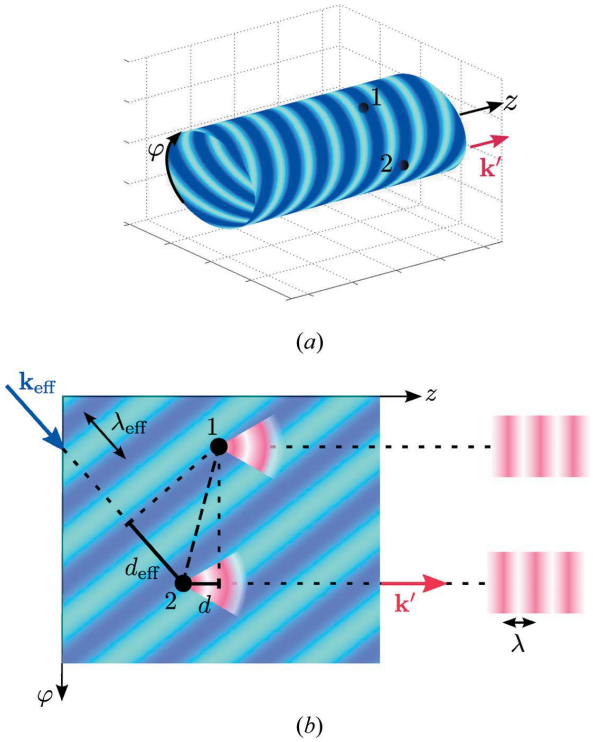

Figure 2
The twisted Bragg/von Laue condition. (*a*) Incoming twisted-wave component restricted to a cylindrical surface containing atoms 1 and 2. (*b*) Diffraction at the two atoms in the axial direction, projected onto the axis/angle coordinate plane. When diffracted from atom 2, incoming and outgoing radiation must travel an additional path in this coordinate plane relative to atom 1. Resonance occurs when the phase shift along this path is an integer multiple of 2π.

3. Bragg/von Laue condition for twisted X-rays

To find the condition for constructive interference, we first note that the twisted wave (1) contains contributions with the three angular wavenumbers $\alpha+1$, $\alpha-1$ and α [equation (8)]. Consider the $\alpha+1$ component and two atoms on a helix, labeled 1 and 2, separated by a rotation angle $\Delta\varphi$ and an axial displacement Δz. Interference is related to the additional path in Fig. 2 that the incoming and outgoing wave must travel to pass through atom 2 as compared to atom 1. In the classical Bragg law, incoming and outgoing waves have the same wavelength and so the phase difference can be expressed in terms of the total path length.

But here *two* wavelengths are present: the wavelength λ of the outgoing plane wave, and the 'effective wavelength' $\lambda_{\rm eff}$ of the incoming twisted-wave component when viewed as a plane wave on the (φ, z) coordinate plane. The total phase difference along the path is $2\pi[(d_{\rm eff}/\lambda_{\rm eff})+(d/\lambda)]$, where $d_{\rm eff}$ is the distance of the two atoms in the (φ, z) plane and d is the distance in the direction of the outgoing wavevector (*e.g.* when the latter agrees with the axial direction, axial distance). Resonance occurs when the phase difference is an integer multiple of 2π, that is to say if

$$\frac{d_{\rm eff}}{\lambda_{\rm eff}}+\frac{d}{\lambda}=n \text{ for integer } n. \qquad (2)$$

We note that the resonance, which came from a twisted-wave component with one angular wavenumber, cannot be canceled by the contributions from the other two angular wavenumbers because these are associated with different polarization directions. The von Laue form of equation (2) is

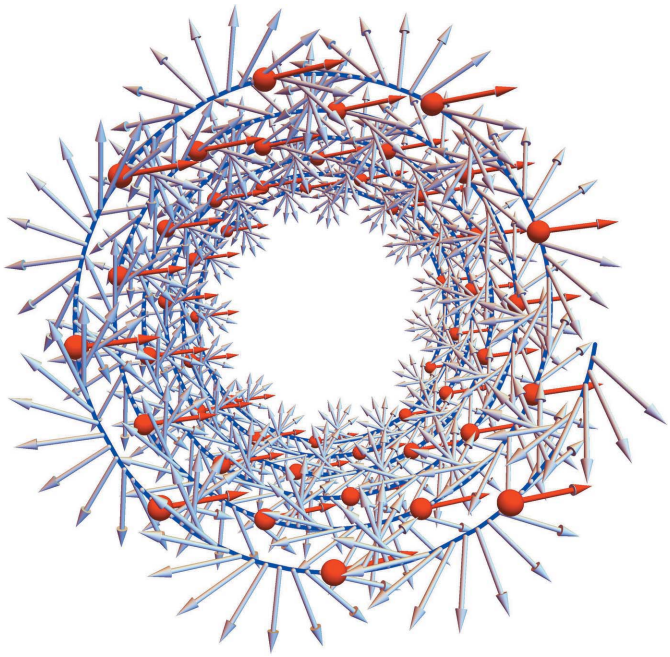

Figure 3
View down the axis of a twisted wave (parameters of Fig. 1). Electric field vectors evaluated at the red atoms also shown in red. Simultaneous resonance of all the atoms is seen by noting that the projections of the red vectors on a plane perpendicular to the axis are all parallel.

electronic reprint

$$\mathbf{k}_{\rm eff} \cdot \begin{pmatrix} \Delta\varphi \\ \Delta z \end{pmatrix} - \mathbf{k}' \cdot \begin{pmatrix} \Delta x \\ \Delta y \\ \Delta z \end{pmatrix} = 2\pi n, \quad n \text{ integer}, \qquad (3)$$

where $\mathbf{k}_{\rm eff} = (\alpha + 1, \beta)$ is the effective wavevector of the incoming twisted-wave component on the (φ, z) plane, $\mathbf{k}'$ is the three-dimensional wavevector of the outgoing (far-field) plane wave, and $(\Delta\varphi, \Delta z)$ and $(\Delta x, \Delta y, \Delta z)$ are, respectively, the difference vectors between atom 2 and atom 1 in the (φ, z) plane and in three-dimensional space.

In Fig. 2 we have only pictured two atoms. But for any helical structure, condition (3) or equation (2) is satisfied simultaneously for all pairs of atoms provided the outgoing wavevector points in an axial direction and the incoming twisted-wave parameters are chosen appropriately (see Appendix *A*). Resonance is illustrated in Fig. 3. The electric field vectors at all atoms, projected onto a plane perpendicular to the axis, are parallel. If, instead of considering a structure that is the orbit of a single atom under the helical group, we had considered the orbit of a collection of atoms, each atom in the collection would be in resonance with all its copies. This is precisely analogous to the situation in crystal diffraction.

4. Structure determination

The remarkable resonance effects of twisted waves with helical structures suggest a promising X-ray method of structure determination. Send twisted waves onto a helical structure. When the twisted waves and the helical structure are axially aligned, and the outgoing radiation is recorded in the axial direction, the radiation exhibits sharp discrete peaks with respect to the radiation parameters α and β. Fig. 4 shows such a simulated diffraction pattern on parameter space, for a typical helical protein crystal of interest, the Pf1 virus. In the simulation we assumed elastic (Thomson) scattering. The pattern is seen to consist of double peaks arranged on a certain lattice. The location of the peaks can be easily derived, in closed form, from the twisted von Laue condition (see Appendix *A*). The vanishing of the signal elsewhere can be explained by a generalization of the Poisson summation

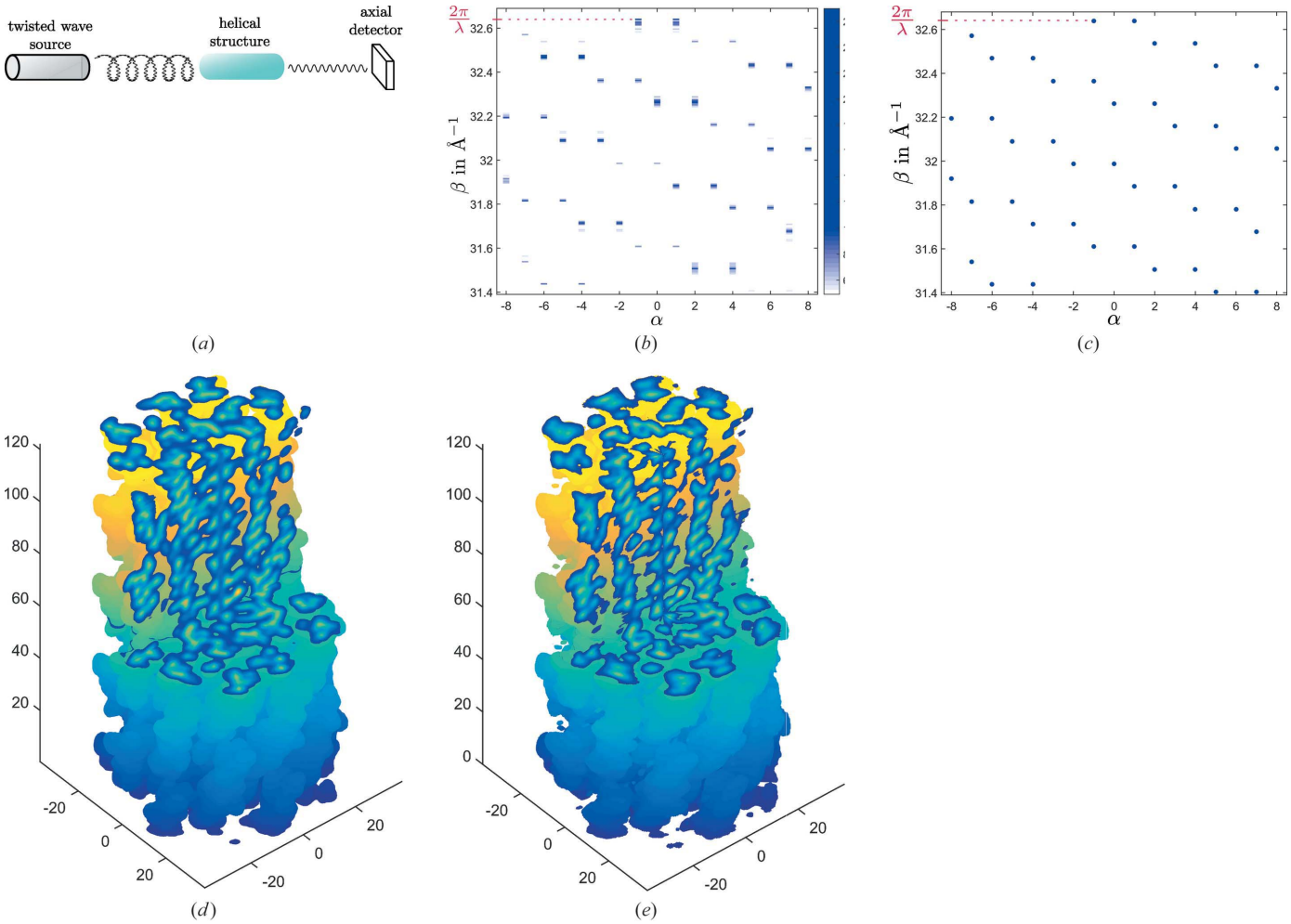

Figure 4
Structure prediction with twisted X-rays. (*a*) Hypothetical setup of twisted X-ray source, structure and detector. (*b*) Simulated axial diffraction signal of Pf1 virus depending on the incoming twisted-wave parameters α and β. The (α, β) plane is the analog of the Ewald sphere. (*c*) Theoretical peak locations from the twisted von Laue condition. (*d*) Model of the true electron density of Pf1 based on data from the Protein Data Bank, PDB entry 1pfi (Liu & Day, 1994). (*e*) Reconstructed electron density obtained from the diffraction data as in (*b*) *via* a phase retrieval algorithm based on work by Elser (2003).

electronic reprint

formula due to Weil (1964) which originated from questions in number theory (see Friesecke *et al.*, 2015).

The left (or right, respectively) part of the double peaks arises from the $(\alpha + 1)$ [or $(\alpha - 1)$, respectively] component of the twisted wave. The α component does not contribute because it is axially polarized and – as is familiar from classical X-ray theory – the outgoing signal in the direction of the incoming polarization vanishes. We remark that scalar models of the incoming radiation as customary in discussions of OAM beams do not suffice to fully understand twisted X-ray diffraction. For example, modeling a twisted wave (1) by a scalar cylindrical wave of angular wavenumber α would predict, instead of double peaks, single peaks at their midpoint. The double peaks reflect the nontrivial vectorial nature of twisted X-rays.

Structure prediction from the diffraction pattern now works in exactly the same way as in the crystal case. The electron density of the unit cell is decomposed into scalar cylindrical waves instead of plane waves [see Appendix *A*, equation (12)], and is completely determined by its complex expansion coefficients whose magnitude can be inferred from the diffraction peak intensities. As in X-ray crystallography, the phases of these coefficients are lost. This phase problem can be overcome by adapting sophisticated phase retrieval algorithms developed for the crystal case. In Fig. 4 we obtained the structure of the Pf1 virus from its simulated diffraction pattern to a remarkable level of detail and accuracy, using a modest number of peak intensities, bias-free random initial phases, and no prior structural information.

5. Conclusions

We have shown on the level of simulation that twisted X-rays, which carry orbital angular momentum, would be a very promising tool for determining the detailed atomic structure of compounds with helical architecture. Incoming twisted X-rays, unlike the incoming plane waves used in X-ray fiber diffraction, resolve not just the axial but also the angular symmetry into sharp peaks.

While it is beyond the scope of this paper to speculate about X-ray machine design, we note that axial detection may necessitate the use of alignment by magnetic fields, as currently used in fiber diffraction, or confinement in a capillary. A temporal analog of the powder method may be useful, in which resonance only occurs occasionally. We note the important point that rotation of the structure about its axis does not change the diffraction pattern for our method, unlike in fiber diffraction.

APPENDIX *A*
Methods

A1. Modeling and design equations

The waveform in equation (1) was obtained from our design equations, which we present in this section. We do this in the general context of an arbitrary discrete Abelian group, so it applies to net (*i.e.* two-dimensional), rod (*i.e.* one-dimensional with an axial translation) or helical structures.

The incoming radiation is modeled as a time-harmonic solution $\mathbf{E}_0(\mathbf{x})\exp(-i\omega t)$ of Maxwell's equations, *i.e.*

$$\Delta\mathbf{E}_0 = -(\omega^2/c^2)\mathbf{E}_0, \;\; \mathrm{div}\,\mathbf{E}_0 = 0, \tag{4}$$

which is to be designed to resonate with the (unknown) structure.

Consider any electronic density $\rho(\mathbf{y})$, $\mathbf{y} \in \mathbb{R}^3$, and a classical model of the electrons driven by the incoming fields and producing the well known outgoing Lienard–Wiechert fields (Griffiths, 1999). Pass to the non-relativistic limit, superpose fields from all the electrons and make the far-field approximation X-ray wavelength $\ll$ sample diameter $\ll$ distance between sample and detector, Fresnel number $\ll 1$. Under these assumptions, the outgoing radiation in the far-field is given by

$$\mathbf{E}_{\mathrm{out}}(\mathbf{x}, t) = -c_{e\ell}\,\frac{\exp\{i[\mathbf{k}'(\mathbf{x})\cdot\mathbf{x} - \omega t]\}}{|\mathbf{x} - \mathbf{x}_c|} \times \left[\mathbf{I} - \frac{\mathbf{k}'(\mathbf{x})}{|\mathbf{k}'(\mathbf{x})|}\otimes\frac{\mathbf{k}'(\mathbf{x})}{|\mathbf{k}'(\mathbf{x})|}\right]\int_{\mathbb{R}^3}\mathbf{E}_0(\mathbf{y})\rho(\mathbf{y})\exp[-i\mathbf{k}'(\mathbf{x})\cdot\mathbf{y}]\,\mathrm{d}\mathbf{y}, \tag{5}$$

with the outgoing wavevector familiar from standard X-ray theory, $\mathbf{k}'(\mathbf{x}) = (\omega/c)(\mathbf{x} - \mathbf{x}_c)/|\mathbf{x} - \mathbf{x}_c|$. [The diffraction model (5) is standard though only special cases are usually given in textbooks.] Here, $c_{e\ell}$ is a universal constant depending on the charge and mass of the electron, $\mathbf{x}_c$ is a typical point in the illuminated region of the sample, $\mathbf{I}$ is the 3×3 identity matrix and $\mathbf{a}\otimes\mathbf{b}$ denotes the 3×3 matrix A with entries $A_{ij} = a_i b_j$. When the electrons are modeled by point charges, (5) reduces to geometric scattering as underlying the derivation of the twisted Bragg/von Laue condition. For incoming plane waves, the integral is the usual scattering factor (Fourier transform of ρ) multiplied by the incoming polarization, and can be derived from non-relativistic quantum electrodynamics (Santra, 2009). Note that $|\mathbf{k}'| = |\mathbf{k}|$ which implies that the photon energy is conserved. Therefore, the model (5) describes elastic or Thomson scattering.

The remarkable discrete diffraction patterns of crystals under plane-wave radiation come mathematically from the behavior of the above integral term, as captured by the Poisson summation formula. The fundamental reason, which we note and exploit in this paper, is that plane waves have a continuous symmetry which mirrors the discrete translation symmetry of crystals, namely that for any vector $\mathbf{a}$, $\mathbf{E}_0(\mathbf{x} + \mathbf{a})$ differs from $\mathbf{E}_0(\mathbf{x})$ by just a phase factor.

Translations are a special case of isometries of three-dimensional space. The Euclidean group of isometries consists of elements $g = (\mathbf{R}|\mathbf{c})$ acting on points in $\mathbb{R}^3$ according to the rule $g(\mathbf{x}) = \mathbf{R}\mathbf{x} + \mathbf{c}$ and on vector fields *via* $(g\mathbf{E}_0)(\mathbf{x}) = \mathbf{R}\mathbf{E}_0[\mathbf{R}^{\mathrm{T}}(\mathbf{x} - \mathbf{c})]$, where $\mathbf{R}$ is any orthogonal 3×3 matrix and $\mathbf{c} \in \mathbb{R}^3$. The translation symmetry of plane waves has a natural analog for any subgroup G of the Euclidean group, namely that

$$(g\mathbf{E}_0)(\mathbf{x}) = \chi_g\mathbf{E}_0(\mathbf{x}) \tag{6}$$

electronic reprint

for some complex number χ_g and all g in G. Equation (6) together with (4) are our design equations. In words, the incoming radiation is simultaneously an eigenfunction of the group (with eigenvalues χ_g) and a divergence-free eigenfunction of the Laplacian (with eigenvalue $-\omega^2/c^2$). For the translation group $G = \{(\mathbf{I}|\mathbf{a}) : \mathbf{a} \in \mathbb{R}^3\}$ the design equations (4), (6) give plane waves. They are the right waves for analyzing crystals, *i.e.* structures whose atomic positions are generated by a discrete translation group. Analogously, solutions to the design equations for another continuous group G are right when the atomic positions are generated by some discrete subgroup of G. Of particular relevance for this paper is Volume E of the *International Tables for Crystallography* which contains the subperiodic groups, *i.e.* those that lack three linearly independent translations.

A2. Twisted waves

We now consider the case of the (continuous) helical group G, which yields the right radiation for helical structures and consists of the elements $(\mathbf{R}|\mathbf{c})$ with $\mathbf{R}$ any rotation about a fixed axis and $\mathbf{c}$ any translation along the axis. The design equations require that

$$\mathbf{R}_\theta \mathbf{E}_0(r, \varphi - \theta, z - \tau) = \chi_{\theta,\tau}\mathbf{E}_0(r, \varphi, z) \tag{7}$$

for all real θ and τ, where (r, φ, z) are cylindrical coordinates with respect to the axis and $\mathbf{R}_\theta$ is a rotation matrix like the one appearing in equation (1) but with φ replaced by θ. Combining two group elements and applying equation (7) either to the combined element or to both elements separately shows that $\chi_{\theta+\theta',\tau+\tau'} = \chi_{\theta,\tau}\chi_{\theta',\tau'}$, and hence $\chi_{\theta,\tau} = \exp[-i(\alpha\theta + \beta\tau)]$ for some integer α and some real β. Evaluation of equation (7) at $\varphi = \theta$, $z = \tau$ gives $\mathbf{E}_0(r, \varphi, z) = \exp[i(\alpha\varphi + \beta z)]\mathbf{R}_\varphi \mathbf{E}_0(r, 0, 0)$. Maxwell's equations for this waveform reduce to a system of three coupled ordinary differential equations which decouple by a unitary transformation into three Bessel equations, leading to equation (1). For more details see Friesecke *et al.* (2015). Calculating the associated magnetic field is elementary, thanks to the general formula $\mathbf{B} = -(i/\omega)\,\mathrm{curl}\,\mathbf{E}$. The result is that $\mathbf{B}$ is also of the form of equation (1) but with $\mathbf{n}$ replaced by $(1/\omega)(0, \gamma, \beta) \times \mathbf{n}$.

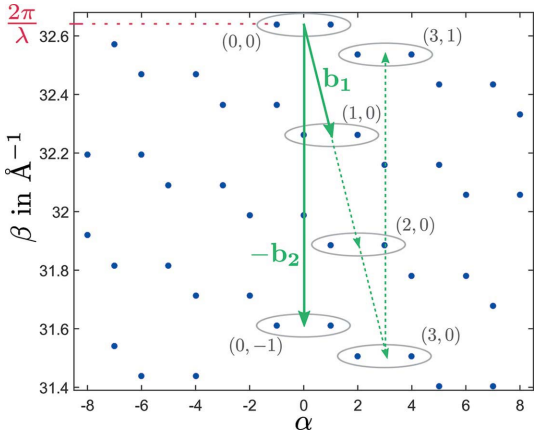

Figure 5
Predicted peak locations, equation (11), with indices (i', j') for Pf1 virus. The reciprocal basis vectors in (11) are $\mathbf{b}_1$ and $\mathbf{b}_2$.

A3. Twisted Bragg condition

The derivation of equations (2)–(3) rests on the following decomposition of the twisted-wave equation (1) into angular wavenumbers $\alpha + 1, \alpha - 1, \alpha$:

$$\mathbf{E}(r, \varphi, z, t) = \exp[i(\beta z - \omega t)]\Big\{\exp[i(\alpha + 1)\varphi]\mathbf{n}_+ J_{\alpha+1}(\gamma r) + \exp[i(\alpha - 1)\varphi]\mathbf{n}_- J_{\alpha-1}(\gamma r) + \exp(i\alpha\varphi)\mathbf{n}_0 J_\alpha(\gamma r)\Big\} \tag{8}$$

where the polarization vectors $\mathbf{n}_+$, $\mathbf{n}_-$, $\mathbf{n}_0$ are the columns of the second matrix in equation (1). Equation (8) follows from an easily checked 'intertwining relation' between the rotation matrix in (1), which we shall denote $\mathbf{R}_\varphi$, and its diagonalization $\mathbf{D}_\varphi = \mathrm{diag}\,[\exp(i\varphi), \exp(-i\varphi), 1]$, namely that $\mathbf{R}_\varphi \mathbf{N} = \mathbf{N}\mathbf{D}_\varphi$, where $\mathbf{N}$ is the second matrix in equation (1). We note that the three contributions in equation (8) are not themselves solutions to Maxwell's equations because only their sum is divergence-free.

A4. Von Laue form of the twisted Bragg condition

Let us express the twisted Bragg condition in the von Laue form, *i.e.* in terms of the wavevector $\mathbf{k}_{\rm eff} = (\alpha + 1, \beta)$ of the incoming twisted-wave component on the (φ, z) plane and the three-dimensional wavevector $\mathbf{k}'$ of the outgoing (far-field) plane wave. The wavelengths are $\lambda_{\rm eff} = 2\pi/|\mathbf{k}_{\rm eff}|$ and $\lambda = 2\pi/|\mathbf{k}'|$. The distance $d_{\rm eff}$ in the plane (Fig. 2) is the projection of the dashed line onto the direction of the effective incoming wavevector, *i.e.* $d_{\rm eff} = (\mathbf{k}_{\rm eff}/|\mathbf{k}_{\rm eff}|) \cdot (\Delta\varphi, \Delta z)$, where the latter is the difference vector between atom 2 and atom 1 in this plane. Likewise, $d = -(\mathbf{k}'/|\mathbf{k}'|) \cdot (\Delta x, \Delta y, \Delta z)$, where $(\Delta x, \Delta y, \Delta z)$ is the difference vector between atom 2 and atom 1 in three-dimensional space. Substitution into (2) gives equation (3).

A5. Predicted peak locations

The pattern in Fig. 4(*c*) was obtained in closed form from the twisted von Laue condition equation (3), as follows. We give the formula for general helical structures of infinite length. The atom positions of such a structure are obtained by applying the integer powers of an n-fold rotation and a screw displacement to a finite set of atoms. The screw displacement consists of a rotation by some angle θ_0 about the helical axis and a displacement by some distance τ_0 along the axis. In cylindrical coordinates, the positions of all copies of the νth atom are $r = r_\nu$ and

$$\begin{pmatrix}\varphi\\ z\end{pmatrix} = \begin{pmatrix}\varphi_\nu\\ z_\nu\end{pmatrix} + i\begin{pmatrix}2\pi/n\\ 0\end{pmatrix} + j\begin{pmatrix}\theta_0\\ \tau_0\end{pmatrix} \bmod \begin{pmatrix}2\pi\\ 0\end{pmatrix}, \tag{9}$$

where i, j are integers, $(r_\nu, \varphi_\nu, z_\nu)$ are the coordinates of the νth atom and $\tilde{\varphi} \bmod 2\pi$ denotes the angle in the interval $0 \le \varphi < 2\pi$ which differs from $\tilde{\varphi}$ by an integer multiple of 2π. The signals of these atoms induced by the $(\alpha + 1)$ component

electronic reprint

of an incoming twisted wave (8) and emitted in an axial direction interfere constructively when the twisted von Laue condition (3) holds for *all* differences $(\Delta\varphi, \Delta z)$ of two atom positions (9). Here the effective incoming wavevector is $\mathbf{k}_{\rm eff} = (\alpha + 1, \beta)$ and the outgoing wavevector is $\mathbf{k}' = (0, 0, 2\pi/\lambda)$, with λ being the wavelength. Thus constructive interference holds if and only if

$$\begin{pmatrix} \alpha+1 \\ \beta - 2\pi/\lambda \end{pmatrix} \cdot \left[i \begin{pmatrix} 2\pi/n \\ 0 \end{pmatrix} + j \begin{pmatrix} \theta_0 \\ \tau_0 \end{pmatrix} \right] = 2\pi n_{ij}, \qquad (10)$$

where n_{ij} is an integer for all integer choices of i and j. Note that the vectors in the square brackets form the helical lattice of the structure, which is a subset of the (φ, z) coordinate plane. Analogously, constructive interference of the signals induced by the $(\alpha - 1)$ component of the twisted wave occurs when equation (10) holds with $\alpha + 1$ replaced by $\alpha - 1$. The solutions to equation (10) and its $(\alpha - 1)$ analog are easily computed, yielding the peak locations

$$\begin{pmatrix} \alpha+\sigma \\ \beta - 2\pi/\lambda \end{pmatrix} = i' \begin{pmatrix} n \\ -n\theta_0/\tau_0 \end{pmatrix} + j' \begin{pmatrix} 0 \\ 2\pi/\tau_0 \end{pmatrix}, \qquad (11)$$

where i' and j' are integers and $\sigma = \pm 1$. The vectors on the right form the reciprocal helical lattice of the structure. The integers i', j' are analogous to Miller indices, and σ indicates the twisted-wave component causing the peak. Fig. 4(*c*) shows the peak locations (11) for the structure parameters θ_0, τ_0 and $n = 1$ of Pf1 virus and the incoming wavelength λ = 0.1925 Å used in the simulation. Note that, conversely, the peak locations (11) uniquely determine the structure parameters θ_0, τ_0 and n (Fig. 5).

A6. Reconstruction

The reconstruction of Pf1 virus from simulated diffraction data (Fig. 4*e*) rests on the following expansion of any electron density $\rho_{e\ell}$ with *helical* symmetry into *cylindrical* waves (which replaces the familiar Fourier expansion of a *periodic* electron density into *plane* waves):

$$\rho_{e\ell}(r, \varphi, z) = \sum_{i',j'} \int_0^\infty \gamma \, {\rm d}\gamma \, G_{i'j'}(\gamma) J_{i'n}(\gamma r) \times \exp\left[i(i'\mathbf{b}_1 + j'\mathbf{b_2}) \cdot \begin{pmatrix} \varphi \\ z \end{pmatrix} \right]. \qquad (12)$$

Here $\mathbf{b}_1$, $\mathbf{b}_2$ are the basis vectors of the reciprocal helical lattice appearing in equation (11), the $G_{i'j'}(\gamma)$ are complex expansion coefficients, and helical symmetry of $\rho_{e\ell}$ means that $\rho_{e\ell}(r, \varphi - a_1, z - a_2) = \rho_{e\ell}(r, \varphi, z)$ for all vectors (a_1, a_2) belonging to the underlying helical lattice [square brackets in equation (10)]. The magnitude of $G_{i'j'}(\gamma)$ is directly proportional to the measurable diffraction peak intensities, γ is the radial wavenumber of the incoming twisted wave, and i', j' are peak labels analogous to Miller indices. As shown in Friesecke *et al.* (2015), the scattering amplitude of the peak with index (i', j') and $\sigma = +1$ in equation (11) is proportional to $|\mathbf{n}_+||G_{i'j'}(\gamma)|$, and that of the peak with $\sigma = -1$ to $|\mathbf{n}_-||G_{i'j'}(\gamma)|$. This reduces structure prediction from twisted X-ray patterns to numerically solving a scalar phase problem, just as in the crystal case.

The method of reconstruction of the structure of the Pf1 virus from the simulated diffraction pattern was as follows: we initialized the phases with bias-free random numbers and applied 5000 steps of Elser's difference map algorithm (Elser, 2003) followed by 100 steps of a Gerchberg–Saxton algorithm (Gerchberg & Saxton, 1972). The incoming twisted X-rays were restricted to wavelengths above λ = 0.1925 Å and angular wavenumbers up to $\alpha = 8$, and the simulations were carried out using *MATLAB*. The resulting reconstructed virus is shown in Fig. 4(*e*).

Acknowledgements

GF was partially supported by DFG through SFB-TR 109. RDJ was supported by AFOSR (FA9550-15-1-0207) and partially supported by ONR (N00014-14-0714), NSF/PIRE (OISE-0967140), the MURI program (FA9550-12-1-0458), and a John Von Neumann visiting professorship at TU Munich. DJ was partially supported by a stipend from Universität Bayern e.V. GF and RDJ thank Dominik Schryvers for helpful information on vortex beams and GF thanks Robin Santra for providing advice on the derivation of X-ray diffraction intensities from quantum electrodynamics.

References

Allen, L., Beijersbergen, M. W., Spreeuw, R. J. C. & Woerdman, J. P. (1992). *Phys. Rev. A*, **45**, 8185–8189.
Arlt, J. & Dholakia, K. (2000). *Opt. Commun.* **177**, 297–301.
Bragg, W. L. (1913). *Proc. R. Soc. A Math. Phys. Eng. Sci.* **89**, 248–277.
Cochran, W., Crick, F. H. & Vand, V. (1952). *Acta Cryst.* **5**, 581–586.
Elser, V. (2003). *J. Opt. Soc. Am. A*, **20**, 40–55.
Friedrich, W., Knipping, P. & von Laue, M. (1912). *Sitzungsber. Math. Phys. Kl. K. Bayer. Akad. Wiss. München*, pp. 303–322.
Friesecke, G., James, R. D. & Jüstel, D. (2015). arXiv: 1506.04240.
Gerchberg, R. W. & Saxton, W. O. (1972). *Optik*, **35**, 237–246.
Griffiths, D. J. (1999). *Introduction to Electrodynamics*, Vol. 3. Upper Saddle River, NJ, USA: Prentice Hall.
Hansen, W. W. (1937). *J. Appl. Phys.* **8**, 282–286.
Juchtmans, R., Béché, A., Abakumov, A., Batuk, M. & Verbeeck, J. (2015). *Phys. Rev. B*, **91**, 094112.
Juchtmans, R. & Verbeeck, J. (2015). arXiv: 1506.00784.
Keen, D. A. & Goodwin, A. L. (2015). *Nature (London)*, **521**, 303–309.
Liu, D. J. & Day, L. A. (1994). *Science*, **265**, 671–674.
Miao, J., Charalambous, P., Kirz, J. & Sayre, D. (1999). *Nature (London)*, **400**, 342–344.
Molina-Terriza, G., Torres, J. P. & Torner, L. (2007). *Nat. Phys.* **3**, 305–310.
Santra, R. (2009). *J. Phys. B At. Mol. Opt. Phys.* **42**, 023001.
Strichartz, R. S. (2003). *A Guide to Distribution Theory and Fourier Transforms.* Singapore: World Scientific.
Stubbs, G. (2001). *Rep. Prog. Phys.* **64**, 1389–1425.
Uchida, M. & Tonomura, A. (2010). *Nature (London)*, **464**, 737–739.
Veenendaal, M. van & McNulty, I. (2007). *Phys. Rev. Lett.* **98**, 157401.
Verbeeck, J., Tian, H. & Schattschneider, P. (2010). *Nature (London)*, **467**, 301–304.
Weil, A. (1964). *Acta Math.* **111**, 143–211.

electronic reprint